DOI: https://doi.org/10.14311/TPFM.2019.020

LARGE-EDDY SIMULATION OF FLOW THROUGH HUMAN LARYNX WITH A TURBULENCE GRID AT INLET

M. Lasota [1], **P. Šidlof** [1, 2]

[1] **Technical University of Liberec, Faculty of Mechatronics, Informatics and Interdisciplinary Studies, NTI Institute, Studentska 2, 461 17 Liberec, Czech Republic**

[2] **Institute of Thermodynamics, Academy of Sciences of the Czech Republic, Dolejskova 5, 182 00 Prague 8, Czech Republic**

Abstract

The upcoming paper brings forward some remarks connected with a turbulence initialization at the inlet of a computational domain. The computational domain is a simplified model of human larynx with vocal folds. As a numerical solution of an airflow through the larynx is applied a Large-Eddy Simulation (LES) approach. Our goal was to induce turbulence fluctuations directly in the subglottal area by using a model of a turbulence grid at inlet. The Reynolds numbers encountered in glottal flow lie in the transitional regime.

Keywords: CFD, LES, vocal folds, OpenFOAM, turbulence grids

1 Introduction

The phonatory process occurs when air is expelled from the lungs through the glottis and the pressure drop causes flow-induced oscillations of the vocal folds. The flow fields created in phonation are highly unsteady and the coherent vortex structures are also generated. Notice that the glottis has the most influence on the creation of the voice's fundamental frequency [20]. The presence of the turbulent flow at the subglottal area is partly supported in [16], where the three canine larynxes were used to measure a turbulence intensity Tu (not phonating) and the Tu into the subglottis was more than 20 % in the shear layer.

This paper presents the results from OpenFOAM (OF) which are obtained with a Large-Eddy Simulation (LES) using second-order finite volume discretization of incompressible Navier-Stokes equations. Large-eddy simulations with different subgrid scale models are executed on a structured mesh. In these cases, only the SGS models which model turbulence via turbulent viscosity and Boussinesq approximation in subglottal and supraglottal area in the larynx are used.

2 Mathematical model

Let a flow variable f be decomposed as $f = \bar{f} + f'$, where $\bar{f}$ is a large scale contribution (resolved) and f' is a small scale contribution (to be modeled). The separation between large grid scale (GS) and small sub-grid scale (SGS) is defined by characteristic length Δ[m]. For the extraction of the large scales, the filtered variable is defined by the convolution integral

$$\bar{f}_i(x_1, x_2, x_3) = \iiint_\Omega \Big[\prod_{j=1}^{3} G_j(x_j, x_j')\Big] f_i(x_1', x_2', x_3') dx_1' dx_2' dx_3', \tag{1}$$

over the entire flow domain Ω, where x_i and x_i' are position of vectors, G is the general filter function. The normalization condition is satisfied if

$$\iiint_\Omega \Big[\prod_{j=1}^{3} G_j(x_j, x_j')\Big] dx_1' dx_2' dx_3' = 1. \tag{2}$$

Plenty of filters exist and the top-hat (or also called volume-averaged box) filter is most frequently used with finite-difference and finite-volume methods, because for finite volume methods, where the flow variable in the approximate solution is constant or varies linearly over the finite volume, the cell-centered value and the local filtered value are then equal for a suitably chosen filter width. The filter is given by

$$G_j(x_j - x_j') = \begin{cases} \dfrac{1}{\Delta_j}, \; |x_j - x_j'| \leq \dfrac{\Delta_j}{2}, \\ 0, \; \textit{otherwise}, \end{cases} \tag{3}$$

hence

$$f_i(x,t) = \frac{1}{\Delta^3}\int_{x_1-\Delta x_1/2}^{x_1+\Delta x_1/2}\int_{x_2-\Delta x_2/2}^{x_2+\Delta x_2/2}$$

$$\times\int_{x_3-\Delta x_3/2}^{x_3+\Delta x_3/2} f(x_1-x_1', x_2-x_2', x_3-x_3')dx_1'dx_2'dx_3', \tag{4}$$

where the filter-width $\Delta = (\Delta x_1 \Delta x_2 \Delta x_3)^{1/3}$ and $\Delta x_1, \Delta x_2, \Delta x_3$ are increments in x_1, x_2, x_3. The space averaging near the wall with the same width of the filter can be used in the case with the strictly the same size of volume cells.

The Navier-Stokes Eqs. for an incompressible flow are presented

$$\frac{\partial}{\partial x_i}(U_i) = 0, \tag{5}$$

$$\frac{\partial}{\partial t}(U_i) + \frac{\partial}{\partial x_j}(U_iU_j) = -\frac{1}{\rho}\frac{\partial}{\partial x_i}(P) + \nu\frac{\partial^2}{\partial x_k \partial x_k}(U_i), \tag{6}$$

where U is a velocity of fluid, P represents dynamic pressure and ν is a kinematic viscosity of fluid [7]. Application of the filtration operator on (5) and (6) yields

$$\frac{\partial}{\partial x_i}(\bar{U_i}) = 0, \tag{7}$$

$$\frac{\partial}{\partial t}(\bar{U_i}) + \frac{\partial}{\partial x_j}(\overline{U_iU_j}) = -\frac{1}{\rho}\frac{\partial}{\partial x_i}(\overline{P}) + \nu\frac{\partial^2}{\partial x_k \partial x_k}(\overline{U_i}), \tag{8}$$

where $\overline{U_iU_j}$ can not be expressed directly [7]. Equation (8) is editted by $+\frac{\partial}{\partial x_j}(\bar{U_i}\bar{U_j})$ to the left and the right side, then

$$\frac{\partial}{\partial t}(\bar{U_i}) + \frac{\partial}{\partial x_j}(\bar{U_i}\bar{U_j}) = -\frac{1}{\rho}\frac{\partial}{\partial x_i}(\overline{P}) + \nu\frac{\partial^2}{\partial x_k \partial x_k}(\overline{U_i}) - \frac{\partial}{\partial x_j}(\tau_{ij}). \tag{9}$$

The term τ_{ij} is the subgrid scale tensor

$$\tau_{ij} = \overline{U_iU_j} - \bar{U_i}\bar{U_j} = -(\overline{u_i'u_j'} + \overline{\bar{U_i}u_j'} + \overline{u_i'\bar{U_j}} + \overline{\bar{U_i}\bar{U_j}} - \bar{U_i}\bar{U_j}), \tag{10}$$

where $-\overline{u_i'u_j'}$ is a Reynolds-stress-like term, $-(\overline{\bar{U_i}u_j'} + \overline{u_i'\bar{U_j}})$ is the Clark term [5] and $\bar{U_i}\bar{U_j} - \overline{\bar{U_i}\bar{U_j}}$ is the Leonard tensor [10]. These SGS tensors need to be modeled. This tensor τ_{ij} represents the effect of the SGS turbulence on the GS flow, carries an influence of the small scales and can not be expressed explicitly [7]. Subgrid scale models for modeling this tensor are presented below.

The Smagorinsky model is based on the idea that small scales are isotropic and therefore Boussinesq hypothesis could be used

$$\tau_{ij} - \frac{1}{3}\delta_{ij}\tau_{kk} = \tau_{ij} - \frac{2}{3}k\delta_{ij} = -2\nu_t\overline{S_{ij}}, \tag{11}$$

where δ_{ij} is the Kronecker delta, k is the SGS kinetic energy, ν_t is kinematic SGS viscosity

$$\nu_t = (C_S\Delta)^2|2\overline{S_{ij}S_{ij}}|^{1/2}, \tag{12}$$

$$\overline{S_{ij}} = \frac{1}{2}\Big(\frac{\partial}{\partial x_j}(\bar{U_i}) + \frac{\partial}{\partial x_i}(\bar{U_j})\Big), \tag{13}$$

where C_S[-] is the Smagorinsky constant, Δ [m] is the filter width and $\overline{S_{ij}}$ is the stress tensor from resolved flow. In LES, a numerically predicted velocity field should capture the effects of the large eddies and the upcoming parameters are essential to set up the case in OF (LESModel-Smagorinsky): C_k, C_e and C_Δ. The dependences are following

$$\mu_t = \rho\nu_t = \rho C_k \Delta\sqrt{k'}, \tag{14}$$

where ν_t has two representations now, (12) defined from the theory and (14) in the form how the ν_t is implemented in OF. The terms in (14) are further written as

$$k' = \sqrt{-b + \frac{\sqrt{b^2+4ac}}{2a}}, \tag{15}$$

$$a = \frac{C_e}{\Delta},\ b = \frac{2}{3}\mathrm{tr}(\bar{\mathbf{S}}),\ c = 2C_k\Delta(\mathrm{dev}(\bar{\mathbf{S}}:\bar{\mathbf{S}}), \tag{16}$$

$$\Delta = C_\Delta V_C^{\frac{1}{3}}, \tag{17}$$

where C_k and C_e are model constants, V_C is the volume of the cell. The values are $C_k = 0.094$, $C_e = 1.048$ and $C_\Delta = 1$ (for 3D) by default. This setting should lead to the value of the Smagorinsky constant $C_S = 0.17$.

In [21] the influence of these parameters on the final coefficient of drag C_D in the steady flow around the bluff body was tested. The result was $C_S = 0.17$, as we refered, and lead to the $C_D = 1.38$, i.e. predicted higher that the physical experiment. The value $C_S = 0.1$ lead to the more acceptable value C_d. Our own benchmark test was based on [12], i.e. a cross-flow over a singular circular cylinder at $Re_D = 2580$. This setting should lead to the value of the Smagorinsky constant $C_S = 0.17$. In [21] the influence of these parameters on the final coefficient of drag C_D in the steady flow around the bluff body was tested. The result was $C_S = 0.17$, as we refered, and lead to the $C_D = 1.38$, i.e. predicted higher that the physical experiment. The value $C_S = 0.1$ lead to the more acceptable value C_d. Our own benchmark test was based on [12], i.e. a cross-flow over a singular circular cylinder at $Re_D = 2580$.

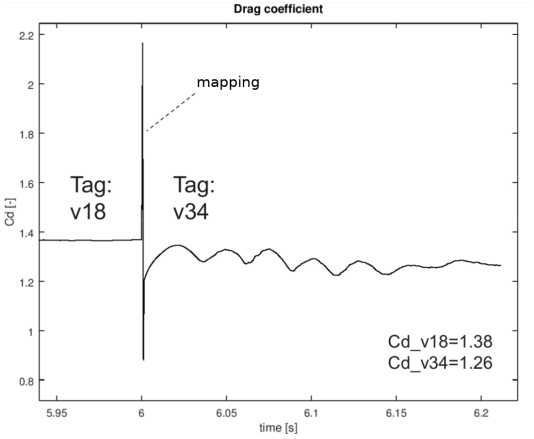

Figure 1: Setting the parameter C_k.

In Fig. 1, where we modified $C_k = 0.094$ (tag v18) to $C_k = 0.047147$ (tag v34) with a goal to decrease C_d to the laboratory value. In other words, the modifications lead to $C_S = 0.1$ and the used $C_k = 0.047147$ is from [11]. The value $C_S = 0.1$ is suitable for a near-wall zone [13].

3 Numerical solution

In this LES study, the central differencing scheme (CDS) is used for spatial discretization of the diffusive term. The CDS can be obtained through a Taylor series expansion where the terms involve derivatives of the second order. The second order CDS is non-dissipative and conservative, which is essential for LES. Upwind-based schemes are not used in LES, because of the production of high numerical dissipation [9]. For the spatial discretization of the convective term, a total variation diminishing scheme (TVD) is used. A numerical method is said to be TVD, if the total variation (TV)

$$TV^{t+\Delta t} = \sum_i |\phi_{i+1}^{t+\Delta t} - \phi_i^{t+\Delta t}| \leq \sum_i |\phi_{i+1}^{t} - \phi_i^{t}| = TV^{t} \tag{18}$$

does not increase in time. Here ϕ is a variable and i is an index of the node. A monotone scheme is TVD and a TVD scheme preserves monotonicity. It does not create any new local extrema within the solution domain. In our case, we have used a high resolution scheme,

$$\phi_f = \underbrace{\frac{1}{2}(\phi_D - \phi_C)}_{CD} = \underbrace{\phi_C}_{upwind} + \underbrace{\frac{1}{2}(\phi_D - \phi_C)}_{anti-diffusive flux} \tag{19}$$

where the term which is called the anti-diffusive flux creates the 2nd order of accuracy (which decreases numerical diffusion, but also leads to unphysical oscillations) [15]. The way to preserve the good properties, i.e. the stability from the 1st order scheme and the accuracy from the 2nd order scheme is to multiply the flux limiter ψ by the anti-diffusive term,

$$\phi_f = \phi_C + \frac{1}{2}\psi(r_f)(\phi_D - \phi_C),\ r_f = \frac{\phi_C - \phi_U}{\phi_D - \phi_C}, \tag{20}$$

where indexes are marked in Fig. 2, D-downwind, C-center, U-upwind, f-face (between C and D) and r_f is taken as the ratio of two consecutive gradients [15]. In this study the flux limiter of the MUSCL TVD scheme was used as the discretization scheme of the convective term,

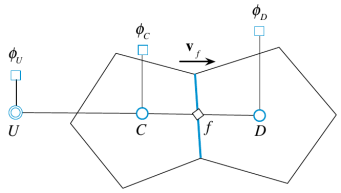

Figure 2: A schematic node locations [15]

$$\psi(r_f) = max(0, min(2r_f, (r_f + 1)/2, 2)) \tag{21}$$

and the CD TVD scheme with $\psi(r_f) = 1$ was used as the discretization scheme of the diffusive term. For the temporal discretization, a second-order backward implicit Euler was used. Since the time steps are small in LES, it is not essential to use a different temporal scheme than second-order.

4 Turbulence initialization and grids

Turbulence generation at the inlet to the computational domain is a known problem of high importance [19]. In Reynolds-Averaged Navier-Stokes (RANS), all quatities defined on boundaries are constants or slowly varying in time. In LES, the variables always include some time-varying and stochastically-varying components of the simulation. Thus, the inlet condition and the correct implementation of the inlet condition have a significant impact on the flow dynamics. Two common methods are shortly described, i.e. precursor and synthesis, and finally we will present a description of the method with an ,,artificial" turbulence grid at the inlet and in the oncoming section our investigations to apply this method on the presented model of the airflow in the domain of vocal folds.

The precursor method means that the turbulence is generated from flow over an auxiliary domain upstream of the inlet boundary and is developed due to a shear. The calculated values of this precursor simulation are saved in time directories and stored in data storage. They are then used in a further simulation, such as initialization. This method that was noticed is not efficient, because an evolution of real turbulence is proportional to the length of a computational domain and it is almost impossible to estimate turbulent length scales as well as turbulence intensities inside the expanded computational domain.

Considering synthesis methods, some form of random fluctuations is created and combined with the mean flow. The white noise prescription at inlet is the simplest solution how to generate some random fluctuations (superimposed on a mean flow) and increase an amplitude of a turbulence intensity, see (22), but the N-S solver destroys characteristics of turbulent flow, because these fluctuations are not correlated [1], [2] and [19]. The data generated do not exhibit any spatial or temporal correlations and the energy is also spread over all wave numbers and due to a lack of large scale structures the turbulence is quickly dissipated [8]. Advanced synthesis techniques are able to generate more realistic fluctuations.
Turbulence intensity Tu is defined as

$$Tu = \sqrt{\frac{1}{3}\frac{\overline{u_i' u_i'}}{\overline{U}^2}} = \frac{\sqrt{\frac{1}{3}(\overline{u_x'^2} + \overline{u_y'^2} + \overline{u_z'^2})}}{\overline{U}}. \tag{22}$$

where $\overline{u_i' u_i'}$ are variances of the components of the velocity, the standard deviations $u_i^{rms} = \sqrt{\overline{u_i' u_i'}}$. Using coarser mesh leads to under-prediction of the maxima, meaning the locations of the maxima are shifted and the peaks are more diffused.

The method used in this paper, the inletGrid method, is a technique of generating turbulence that incorporates a pattern of solid patches, in our case turbulence uniform grids. The flow enters between the solid patches and turbulence is generated due to the shear. These turbulence generating grids produce wakes behind the bars and jets immediately behind the openings. The grid induced turbulence is well understood and turbulent scales are proportional to the grid size [17], [6]. Turbulence grids are used in a wind tunnel for getting different integral length scales and turbulent intensities. The gridInlet technique is a method how to produce grid-generated turbulence as used in wind tunnels, see [4].

5 Mesh and patterns of turbulence grids

The simulation was set up and realized in OpenFOAM version 5.0. The geometry is based on [18] and all of meshes are composed of hexahedral volume cells, exact numbers of volume cells will be specified later. The structured mesh is designed for wall-resolved LES, for a detailed view of the near-wall mesh see Fig. 3. Boundary conditions were specified with the respect to physics in a respiratory tract, i.e. pressure gradient is prescribed. The pressure gradient assures a natural development of flow.

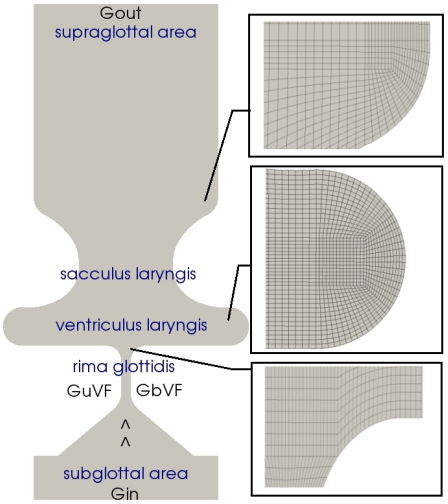

Figure 3: Geometry and mesh

Table 1: Boundary conditions for the velocity $\boldsymbol{U}$, kinematic pressure $P_k = (P/\rho)$.

boundary	$\boldsymbol{U}\,[=]\,m.s^{-1}$	$P_k\,[=]\,m^2.s^{-2}$
Γ_{in}	from flux	300
Γ_{out}	$\frac{\partial \mathbf{U}}{\partial \mathbf{n}} = 0$	0
Γ_{bVF}	$\boldsymbol{U} = 0$	$\frac{\partial P_k}{\partial \mathbf{n}} = 0$
Γ_{uVF}	$\boldsymbol{U} = 0$	$\frac{\partial P_k}{\partial \mathbf{n}} = 0$
Γ_{wall}	$\boldsymbol{U} = 0$	$\frac{\partial P_k}{\partial \mathbf{n}} = 0$
Γ_{in2}	$\boldsymbol{U} = 0$	$\frac{\partial P_k}{\partial \mathbf{n}} = 0$

In the next step Γ_{in} was decomposed into Γ_{in} (inflow) and Γ_{in2} (solid patches), see Fig. 4. The inletGrids were developed to produce wakes immediately behind the bars in order to deform the uniform velocity profile.

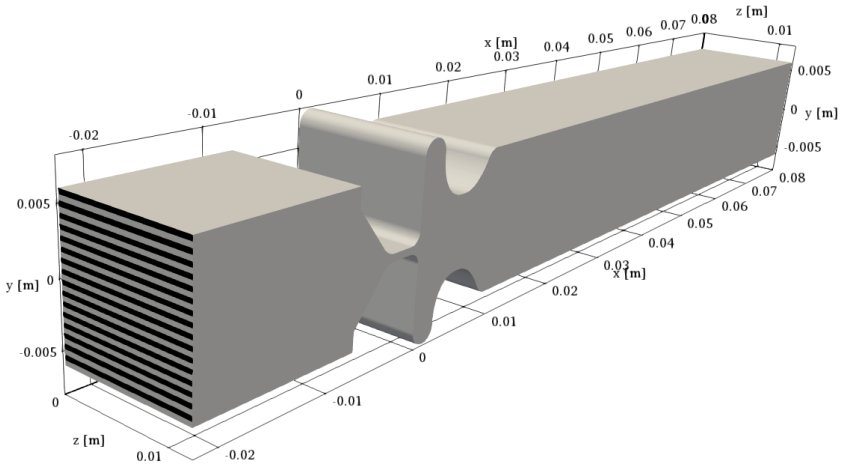

Figure 4: View of the whole vocal folds computational domain for 2D simulations (for 2D, OpenFOAM uses a 3D geometry with a single element per domain thickness). In the figure is obvious a turbulence grid at the inlet to the subglottal region. The inflow is destroyed by uniform grid pattern, where the Γ_{in2} (grid) is represented by black color.

The turbulence grids are presented in this section. The grids G36-G37 are used in 2D simulation cases, see Fig. 5 and the grids G30-G32 appear in 3D cases, see Fig. 6.

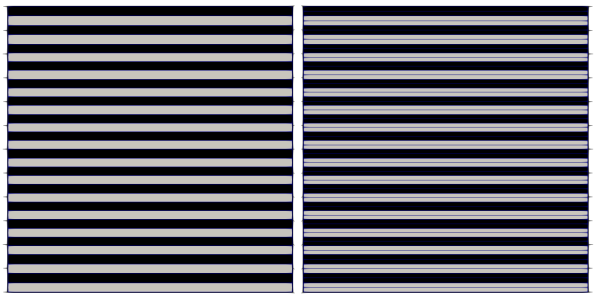

Figure 5: Turbulence grid G36 (left) and G37 (right) used in the simulations to disturb the velocity profile. The G37 has two elements for each bar and each opening, while G36 one element per bar and opening.

Table 2: Details of the used 2D grids (G36-G37); the inlet is LxL, where $L = 0.012$ m; NoGS- Number of Grid Segments

grid	NoGS*	grid spacing (y)	grid spacing (z)
G36	1x32	$0.032L$	–
G37	1x64	$0.016L$	–

Table 3: Details of used 3D grids; the inlet is squared LxL, where $L = 0.012$ m; *NoGS- Number of Grid Segments

grid	NoGS*	grid spacing (y)	grid spacing (z)
G30	8x32	$0.125L$	$0.031L$
G31	24x80	$0.042L$	$0.013L$
G32	24x80	$0.042L$	$0.013L$

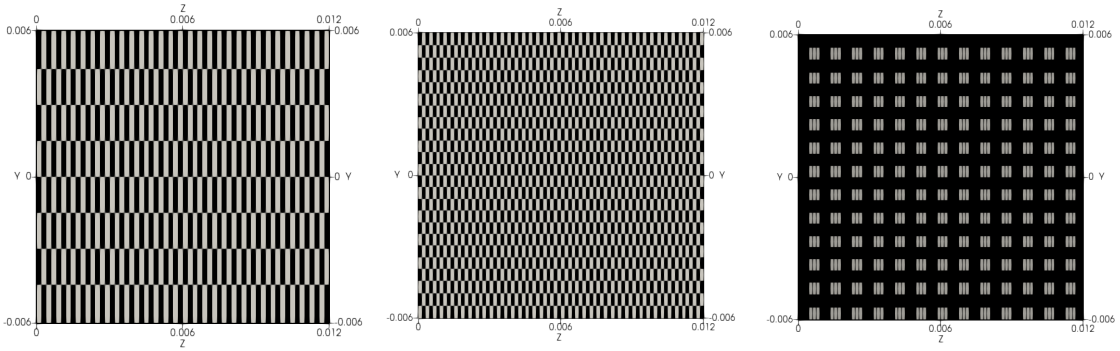

Figure 6: Grid G30 (left), grid G31 (middle), grid G32 (right)

6 Computational results

In this section, numerical simulations of incompressible airflow through the trachea (subglottal-supraglottal area) are shown. Our main interest was to find a way how to increase a turbulence intensity at the subglottal area via turbulence grids, produce wakes immediately behind the bars, deform the uniform velocity profile and identify turbulence fluctuations.

The 2D cases (C023 and C029) with straight and static glottis were simulated, see Tab. 4. The case C023 with the grid G36 has the precisely 2x coarser inlet than the grid G37. In Fig. 7 is shown the comparison for $U_x(t)$ in given probes, the location of each probe is marked in the attached scheme and these probes recorded all components of velocity with a timestep Δt_{write}. Probes E4 and E1 are in the subglottal area and for both cases were not captured any turbulence fluctuations. The representative time interval is ca. $0.002 - 0.004$ s, where the flow is stabilized and influence of the inlet grid should be evident, but turbulence fluctuations were detected merely in P1 (green), located in the jet directly. These green lines are shifted up in the graph for better comprehensibility.

Table 4: Details of the each tested case; $\Delta_{C023} = 2.9992 \cdot 10^{-4}$ m, $\Delta_{C029} = 2.3771 \cdot 10^{-4}$ m; CV-Control Volume

case	dim.	VFposition	type	U_0	dP_k	CV-s	inlet	grid	Δt_{sim}	Δt_{write}
C023	2D	straight	LES	0	300	57k	32x1	G36	$1 \cdot 10^{-6}s$	$1 \cdot 10^{-4}s$
C029	2D	straight	LES	0	300	118k	64x1	G37	$1 \cdot 10^{-6}s$	$1 \cdot 10^{-4}s$

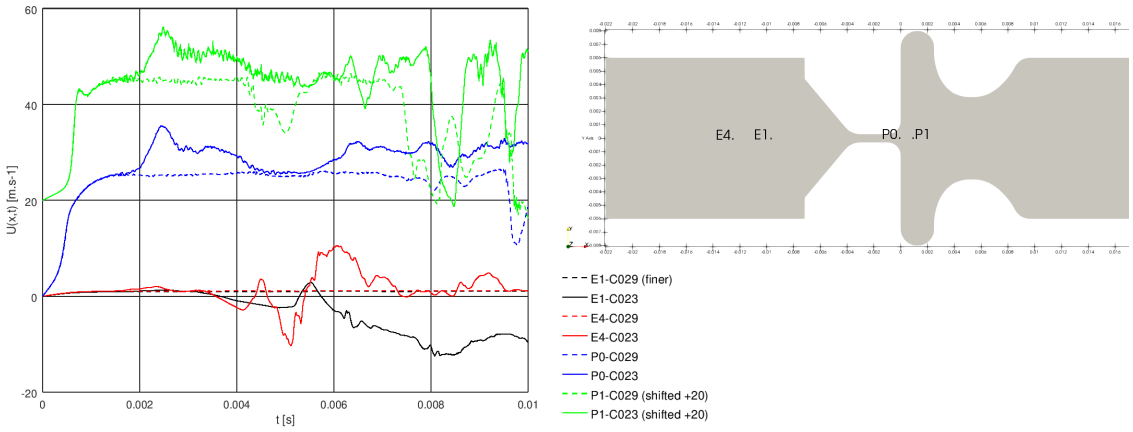

Figure 7: $U(x,t)$ with the straight and static glottis with the finer mesh remained disturbances (as that was expected). This interval is representative for the proof of the pure grid influence, however there are no recognizable turbulence fluctuations.

The Reynolds numbers encountered in glottal flow lie in the transitional regime. The next cases including the grid G37 were tested in the situation with artificially increased pressure gradient in order to simulate the flow in a turbulent regime without doubts. Tab. 5 includes details of cases G030-F030, where G030 is the only case with the uniform velocity profile entering from the inlet. Fig. 7 shows velocity fields in the mid-coronal section of the subglottal area of vocal folds. Fig. 8 shows turbulence intensity fields in $t = 0.01$ s. The influences of used turbulence grid are recognizable at entrance areas at most and then fluctuations are best recognizable close to the inlet, however, further downstream the fluctuations quickly disappear. The nodes located near walls contain higher turbulence intensity. This leads to a conclusion that the turbulence fluctuations in the subglottal area were not attained.

The 3D numerical cases of airflow through the VFs in divergent positions were simulated. The details are presented in Tab. 6.

Table 5: List of used cases; CV-Control Volume, $\Delta = 2.3973 \cdot 10^{-4}$ m

case	dim.	VFposition	type	U_0	dP_k	CV-s	inlet	grid	Δt_{sim}	Δt_{write}
G030	2D	straight	LES	0	300	4.5k	64x1	-	$1 \cdot 10^{-6} s$	$1 \cdot 10^{-4} s$
D030	2D	straight	LES	0	300	4.5k	64x1	G37	$1 \cdot 10^{-6} s$	$1 \cdot 10^{-4} s$
E030	2D	straight	LES	0	3k	4.5k	64x1	G37	$1 \cdot 10^{-6} s$	$1 \cdot 10^{-4} s$
F030	2D	straight	LES	0	30k	4.5k	64x1	G37	$1 \cdot 10^{-6} s$	$1 \cdot 10^{-4} s$

Table 6: List of the used cases (divergent); CV-Control Volume

case	dimension	type	CV-s	inlet	grid	dP_k	$\Delta[m]$	Δt_{sim}	Δt_{write}
C032	3D	LES	230k	8x32	-	300	$2.1968 \cdot 10^{-4}$	$1 \cdot 10^{-5} s$	$2 \cdot 10^{-5} s$
C033	3D	LES	230k	8x32	G30	300	$2.1968 \cdot 10^{-4}$	$1 \cdot 10^{-5} s$	$2 \cdot 10^{-5} s$
C034	3D	LES	2.6M	24x80	G31	300	$8.8819 \cdot 10^{-5}$	$1 \cdot 10^{-5} s$	$2 \cdot 10^{-5} s$

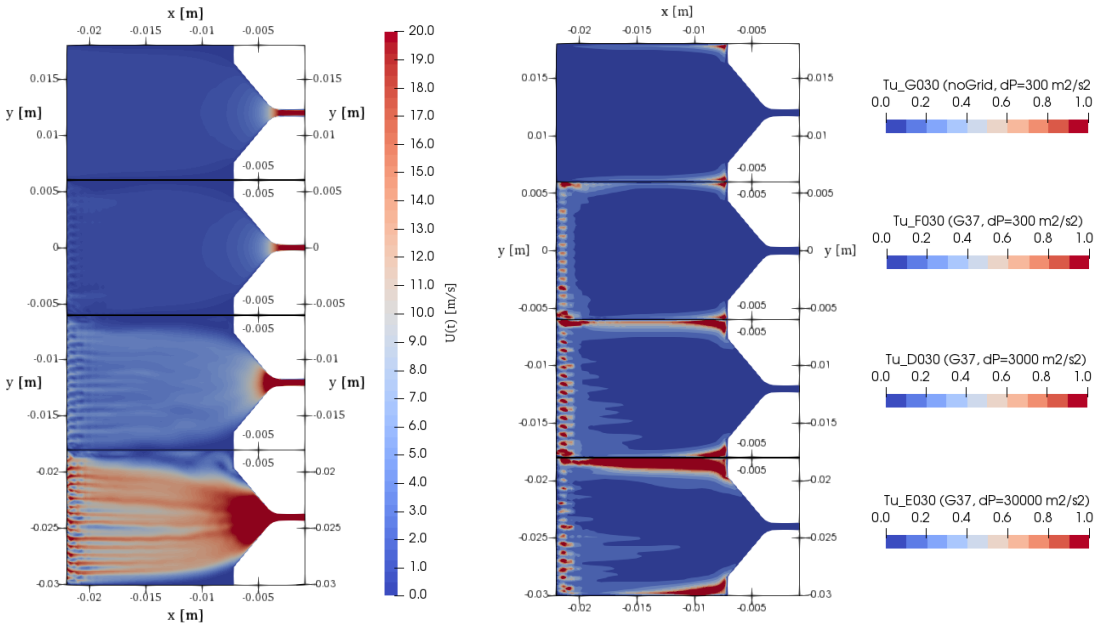

Figure 8: Comparison of the velocity fields (left) and turbulence intensity fields (right) for different kinematic pressure gradients. From top to bottom: G030, F030, D030, E030 (see Tab. 5)

The velocity fields are shown in Fig. 9 (left), where the case without the inlet grid had an uniform flow in the subglottal area, regarding the second case (the grid was added) the disturbances were not significant. Hence, the finer patterns of inlet grids were used. The velocity field at supraglottal area with the grid G32 shows more developed coherent vortex structures. The turbulence intensity fields are also shown on Fig. 9 (right). The higher turbulence intensities are predicted shortly after bars. The case with no grid predicted $Tu = 0.08$ % at the subglottal area and $Tu = 17$ % downstream of the glottal constriction. The case C033 with the G30 (the 2nd case) predicted maximum $Tu = 1$ % located in inlet corners, the situation at supraglottal region is similar to the previous case. The case C034 with the G31 predicted $Tu = 3 - 6$ %. This suggests that the case C034 with the grid G31 produced more turbulent energy than the G30 and prolong the vortices in the supraglottal area (unfortunately two factors were changed here: the mesh and the inlet grid). The Fig. 10 has captured velocity fields in mid-sagittal sections with a complex 3D flow field from the glottis further to the downstream.

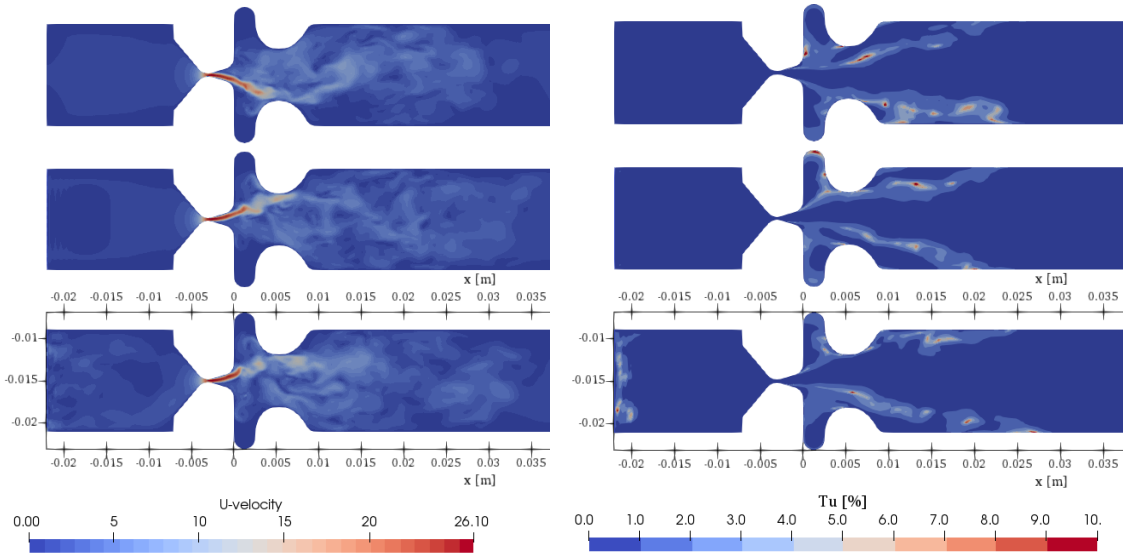

Figure 9: Velocity (left) and turbulence intensity field in mid-coronal section in time $t = 10$ ms: C032 (top), C033, C034 (bottom)

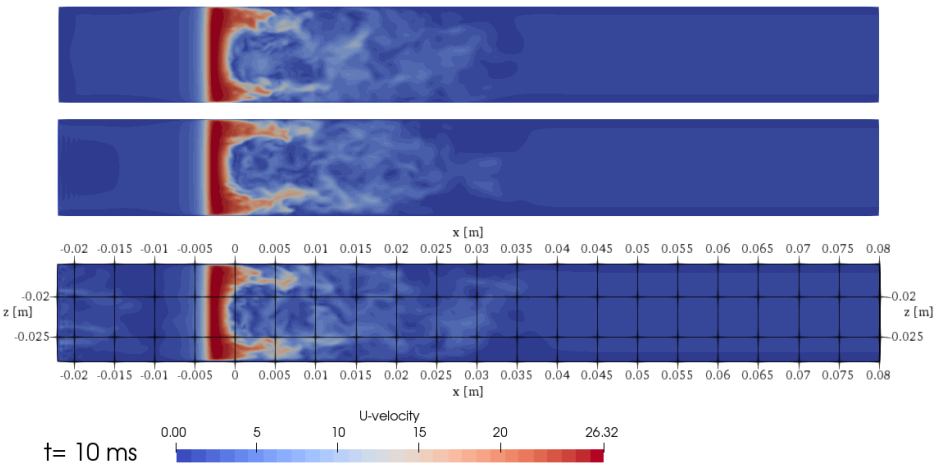

Figure 10: Velocity field in mid-sagittal section in time $t = 10$ ms: C032 (top), C033, C034 (bottom)

The 3D case with presribed motion of the vocal folds (C035) is compared with the (no Motion) case (C034). The details of the mentioned cases are findable in Tab. 7. The kinematics of the vocal folds have been allowed for a two degrees of freedom with sinusoidal displacement of the VF margins in the medial-lateral direction. In (23) and (24) are used these variables: w_{1b} and w_{2b} are positions of the points in $t = 0$ s for lower margin of VF (the straight position of VF, $w_{1b} = w_{2b}$, is captured on Fig. 11 (left) and the position of VF with predeformed shapes, which are in starting state for C034 (static) and C035 (dynamic), is on Fig. 11 (right)). For the upper margin of VF are mentioned points mirrored to positive coordinates (w_{1u} and w_{2u}), $A_1 = A_2 = 0.3{\cdot}10^{-3}$ m represent amplitudes of oscilation and $f_1 = f_2 = 100$ Hz are frequencies of vibration. The paralysis of the upper or the lower VF were not included. ξ is the phase difference $\xi = \pi/2$. $m(z)$ is the anterior-posterior modulation function leading the opening of glottal area, see (25), where $L = 0.012$ m.

Table 7: List of the mentioned cases; CV-Control Volume

case	dim.	type	CV-s	mov.	inlet	grid	dP_k	Δ[m]	Δt_{sim}	Δt_{write}
C034	3D	LES	2.6M	-	24x80	G32	300	$8.8819 \cdot 10^{-5}$	$1 \cdot 10^{-5} s$	$2 \cdot 10^{-5} s$
C035	3D	LES	2.6M	M030	24x80	G32	300	$8.8819 \cdot 10^{-5}$	$1 \cdot 10^{-5} s$	$2 \cdot 10^{-5} s$

$$w_1(z,t) = w_{10} + A_1(1 - m(z)) + m(z)A_1 \sin(2\pi f t + \xi), \tag{23}$$

$$w_2(z,t) = w_{20} + A_2(1 - m(z)) + m(z)A_2 \sin(2\pi f t), \tag{24}$$

$$m(z) = \sin\left(\frac{\pi z}{L}\right). \tag{25}$$

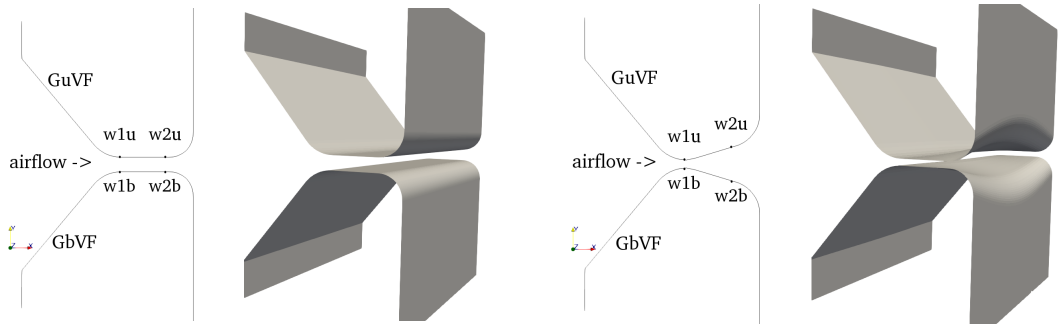

Figure 11: The straight shape of VF (left), the divergent and starting position of VF (right).

The Fig. 12 compares the velocity fields in the coronal section of the simplified larynx geometry between the case with the shape of VF in divergent position and the case with convergent-divergent position of VF (in motion). The left capture is the velocity field gained in $t = 0.005$ s, i.e. almost with the maximum gap (for the dynamic case C035) and the right capture is gained in divergent positions of VF (after a one cycle of oscilation for the dynamic case C035). The velocity fields

show some disturbances at subglottal area caused by turbulence grid G32, air jets formed by glottal constrictions and large vortex structures in supraglottal areas. In Fig. 13, considering the shape of the flow in the glottis (C035) the jet was just bent in the transverse plane direction, that is the reason why the shape of the red region seems dissimilar to the C034. The subglottal areas were analysed by plotted velocity profiles and the results are shown in Fig. 14 shows the situation after a one period of oscillation. The red lines are velocity profiles in the case with uniform airflow (without using a turbulence grid). The disturbances are after one period of oscillation are presented in the whole subglottal region.

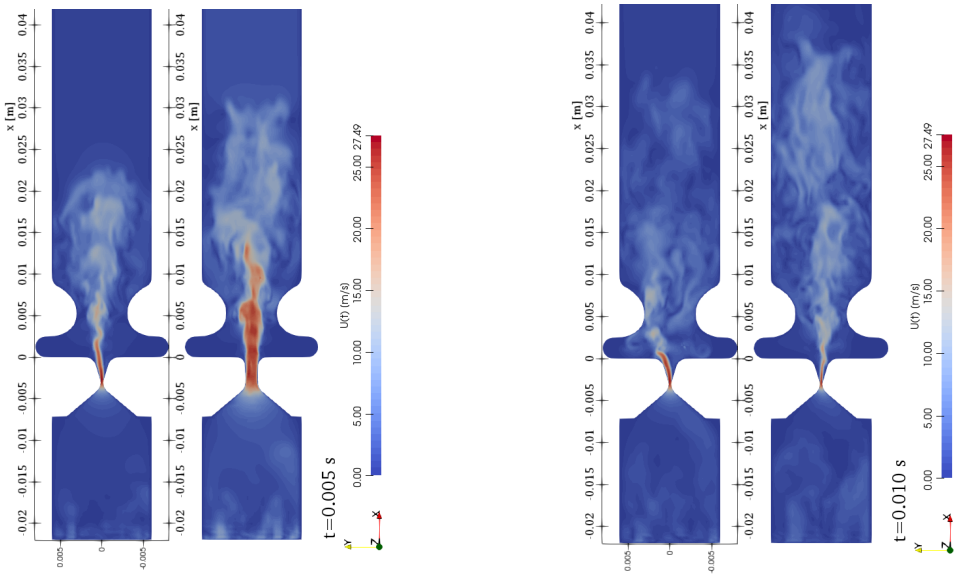

Figure 12: Velocity field in time 5 ms (left) and 10 ms (right); C034 (always on the left side when a pair of captures is presented)

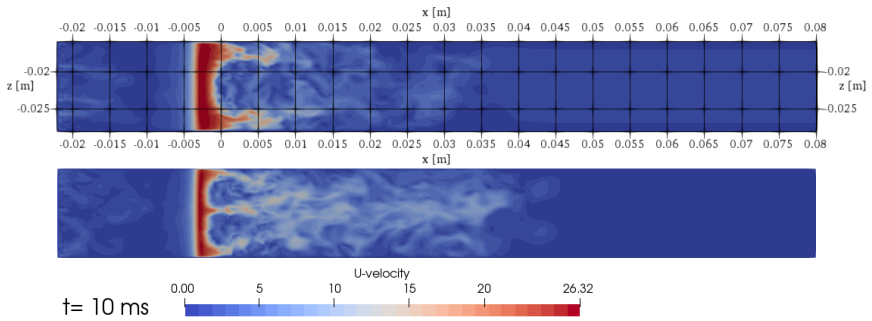

Figure 13: Velocity field in mid-sagittal section in time $t = 10$ ms: C034 (top) and C035 (bottom)

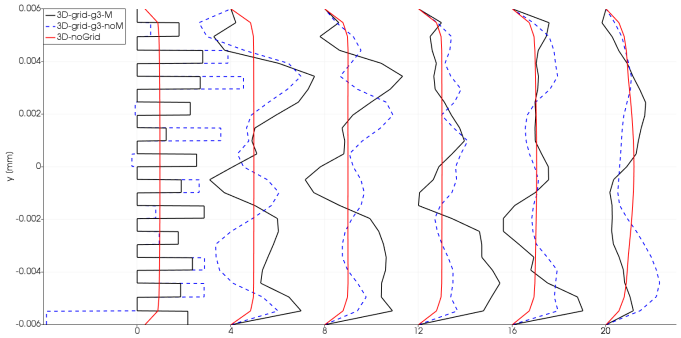

Figure 14: Velocity profile, blue dashed: C034 (3D-grid-g3-noM), black: C035 (3D-grid-g3-M); $t = 10$ ms; The lines are shifted up for better comprehensibility in x-axis and the positions of velocity profiles are $x/L = 0$, 1/6, 1/3, 1/2, 3/4 and 1.

7 Conclusions and discussion

The correct description of the initial turbulence is indisputably essential for accurate results from LES simulations. The inletGrid method helped to generate some relatively small disturbances in velocity fields at subglottal areas, but turbulence fluctuations were not observed in our cases (unlike the turbulence fluctuation downstream of the glottal constriction). Initial disturbances were damped before they reached the glottis, i.e. the flow became laminar. The explanation of this fenomena may lie in the fact, that the turbulence spots are inhibited due to local-space averaging in LES. The locations of the turbulence spots are a characteristic of the high spatial frequency, which is eliminated by low-pass filtering. For further investigation it is recommended to use a suitable mechanism, such as artificial forcing or mapping the values from experimental datasets as shown in Fig. 15, where to test the influence of the initial conditions, an auxiliary LES simulation of flow in a straight rectangular channel at similar Reynolds number, was performed. In details, the Fig. 15 shows the results with $Re_\tau = 395$ and $Re_b = 13350$ and two different initial conditions. The left case with $U_0 = 0$ ms^{-1} is shown, where the flow was stabilizated in the laminar mode. The right case was run with initial velocity values based on DNS data (Direct Numerical Simulation, i.e. the N-S eqs. without averaging and approximation) from [14] and turbulence fluctuations were not destroyed by a numerical scheme.

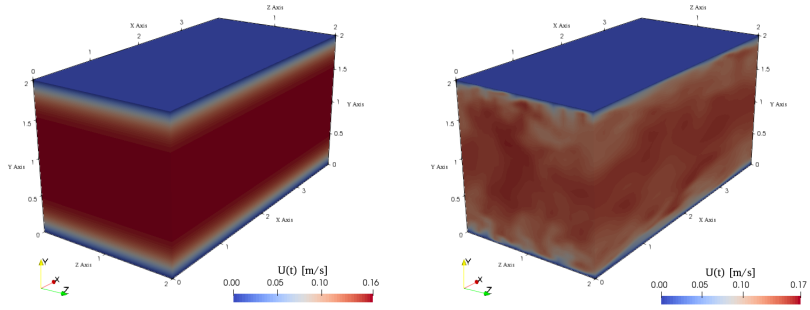

Figure 15: Velocity magnitude in straight channel flow with uniform initial condition (left) and perturbed initial data based on DNS (right)

Acknowledgment

This work was supported by the Ministry of Education of the Czech Republic through the SGS project no. *21176/115* of the Technical University of Liberec.

References

[1] J. Aider and A. Danet. Large-eddy simulation study of upstream boundary conditions influence upon a backward-facing step flow. *Comptes Rendus Mécanique*, 334(7):447–453, 2006.

[2] J. Aider, A. Danet, and M. Lesieur. Large-eddy simulation applied to study the influence of upstream conditions on the time-dependant and averaged characteristics of a backward-facing step flow. *Journal of Turbulence*, (8):N51, 2007.

[3] D. Anderson, J. Tannehill, and R. Pletcher. *Computational fluid mechanics and heat transfer*. CRC Press, 2016.

[4] T. Blackmore, WMJ. Batten, and AS. Bahaj. Inlet grid-generated turbulence for large-eddy simulations. *International Journal of Computational Fluid Dynamics*, 27(6-7):307–315, 2013.

[5] A. Clark, H. Ferziger, and C. Reynolds. Evaluation of subgrid-scale models using an accurately simulated turbulent flow. *Journal of fluid mechanics*, 91(1):1–16, 1979.

[6] P. Davidson. *Turbulence*: an introduction for scientists and engineers Oxford University Press, 2004.

[7] H. Ferziger. Direct and large eddy simulation of turbulence. *Numerical methods in fluid mechanics*, 16:53–73, 1998.

[8] N. Jarrin, S. Benhamadouche, Y. Addad, and D. Laurence. Synthetic turbulent inflow conditions for large eddy simulation. In *Proceedings, 4th International Turbulence, Heat and Mass Transfer Conference, Antalya, Turkey*, 2003.

[9] M. Lasota and P. Šidlof. Large-eddy simulation of internal flow through human vocal folds. In *EPJ Web of Conferences*, volume 180, page 02054. EDP Sciences, 2018.

[10] A. Leonard. Energy cascade in large-eddy simulations of turbulent fluid flows. In *Advances in geophysics*, volume 18, pages 237–248. Elsevier, 1975.

[11] M. Lesieur, O. Métais, and P. Comte. *Large-eddy simulations of turbulence*. Cambridge University Press, 2005.

[12] Ch. Liang and G. Papadakis. Large eddy simulation of pulsating flow over a circular cylinder at subcritical Reynolds number. *Computers and fluids*, 36(2):299–312, 2007.

[13] P. Moin and J. Kim. On the numerical solution of time-dependent viscous incompressible fluid flows involving solid boundaries. *Journal of computational physics*, 35(3):381–392, 1980.

[14] D. Moser, J. Kim, and N. Mansour. Direct numerical simulation of turbulent channel flow up to Re τ= 590. *Physics of fluids*, 11(4):943–945, 1999.

[15] F. Moukalled, L. Mangani, and M. Darwish. The finite volume method in computational fluid dynamics: An introduction with openfoam and matlab, fluid mechanics and its applications, vol, 113,(2015).

[16] L. Oren, S. Khosla, S. Murugappan, R. King, and E. Gutmark. Role of subglottal shape in turbulence reduction. *Annals of Otology, Rhinology and Laryngology*, 118(3):232–240, 2009.

[17] B. Pope. *Turbulent flows*. Cambridge university press, 2000.

[18] R. Scherer, D. Shinwari, J. De Witt, Ch. Zhang, R. Kucinschi, and A. Afjeh. Intraglottal pressure profiles for a symmetric and oblique glottis with a divergence angle of 10 degrees. *The Journal of the Acoustical Society of America*, 109(4):1616–1630, 2001.

[19] R. Tabor and MH. Baba-Ahmadi. Inlet conditions for large eddy simulation: a review. *Computers & Fluids*, 39(4):553–567, 2010.

[20] R. Titze and W. Martin. Principles of voice production, 1998.

[21] F. Tremblay, M. Manhart, and R. Friedrich. LES of flow around a circular cylinder at a high subcritical reynolds number. In *Direct and Large-Eddy Simulation IV*, pages 329–336. Springer, 2001.